

## Chapter 2

# Define and Synthesis on Orbit Diversity

**Abstract** This chapter proposes mathematic models along tool orbits during automated optical finishing process. A numerical method was used to calculate the integration of segments covered by the unit-removal-function (URF). The length covered by the URF was also determined to predict the amount of material removed from a given location on an orbit. Parameters affect the amount and distribution of material removal were analyzed. The curve radius of an orbit should be larger than that of the URF, or dwell time algorithm should also be optimized at a location with a small radius. The turning point of an orbit should be away from the edge of work-piece (at least one radius of the URF), or a turn with large angle should be adopted. For some fractal or random orbits, there are many corners in the orbit. The Harris corner detection algorithm was used to estimate and ensure that the corners were well-distributed over the entire surface. For the effects of curvatures, the maximum material removed is a distance of about 0.5 to the normalized radius of the URF. For the effects of corners, the peak removal is a distance between 0.5 and 1 to a corner. Aside from curvatures and corners, the space between adjacent orbits is another key parameter that affects the amount of removed material. The combined effect of curvatures, corners, spaces, and multiplex-orbit was comprehensively analyzed, and two typical orbits, i.e., spiral and raster orbits were introduced to perform process validation.

### 2.1 Basic Model Along Orbit

Traditional optical finishing techniques rely basically on the skills of craftsmen using the pitch tool, and it is a time-consuming and iterative process [1]. Nowadays, specifications for surface quality, roughness, and the manufacturing efficiency are more stringent, and conventional methods cannot satisfy such demands.

Since the computerized numerical control was introduced into optical finishing industrial practice in the last century, the process based on craftsman-like skills has become more deterministic. Several finishing technologies, such as computer-

controlled optical surfacing [2–4], bonnet polishing [5, 6], ion beam figuring [7, 8], magnetorheological finishing [9–13], magnetorheological jet finishing [14–20], and plasma surface figuring [21], have been developed. Regardless of technology used, however, special finishing tools travel on the work-piece surface along prescribed trajectories, and the surface material are removed due to the pressure and velocity applied, as well as other processing factors.

Some researchers studied the generation of special orbits on different surfaces and the effects of orbits on surface quality. Tam et al. [22, 23] applied a scanning orbit in free-form surface finishing using robots and investigated the effects of adjacent orbit lines, such as scanning, bi-scanning, Hilbert, and Peano orbits. Lartigue et al. [24] presented a method to generate a CNC tool orbit for a smooth free-form surface in terms of planar cubic B-spline. Hauth et al. [25] presented double-spiral tool orbits for polishing process of free-form surface with a continuous, non-overlapping orbit and low variation in distance between adjacent traces of the orbit. Rososhansky et al. [26] treated the tool orbit as a contact problem and presented a method of tool orbit planning for automated polishing.

The mid-spatial frequency (MSF) errors can degrade optical performance of an optical system, including contrast, ensquared energy, and pixel cross-talk, and affect application of optical surface, such as high-power laser systems [27–30]. Dunn and Walker generated a unicursal random tool path and produced a surface with a better power spectral density (PSD) profile than a raster tool orbit, and all other polishing parameters were held constant in their experiment [31]. Other researchers studied the effect on MSF of orbit and discussed how to smooth optical surfaces [32–35].

Actually, several finishing technologies are available, but the material removal mechanisms of these technologies differ. The depth of removed material is usually processed through technical methods and described as linearly related with processing time, relative velocity, pressure, or other parameters. Preston's equation is a basic classical model of finishing, in which the URF at a given location is proportional to engagement pressure  $P(x, y)$  and relative velocity  $V(x, y)$ . It can be expressed as:

$$R(x, y) = K \cdot P(x, y) \cdot V(x, y) \quad (2.1)$$

where  $K$  is the process-dependent coefficient denoted as Preston's coefficient.

The ideal removal function with eccentric rotation motion shows a Gaussian character with peak value in the middle. The Gaussian shape removal function can be given by

$$R_G(x, y) = B \exp[-u \cdot (x^2 + y^2)] \quad (2.2)$$

where  $B$  is the peak removal, and  $u$  is the parameter of the Gaussian shape.

When the tool moves along a part of target orbit (also called regular orbit) with constant velocity (see Fig. 2.1a), the distribution of removal material takes a V-shaped profile, which has maximum removal that gradually decreases as the offset distance increasing (see Fig. 2.1b).  $H_{Gm}$  and  $S_G$  are, respectively, the

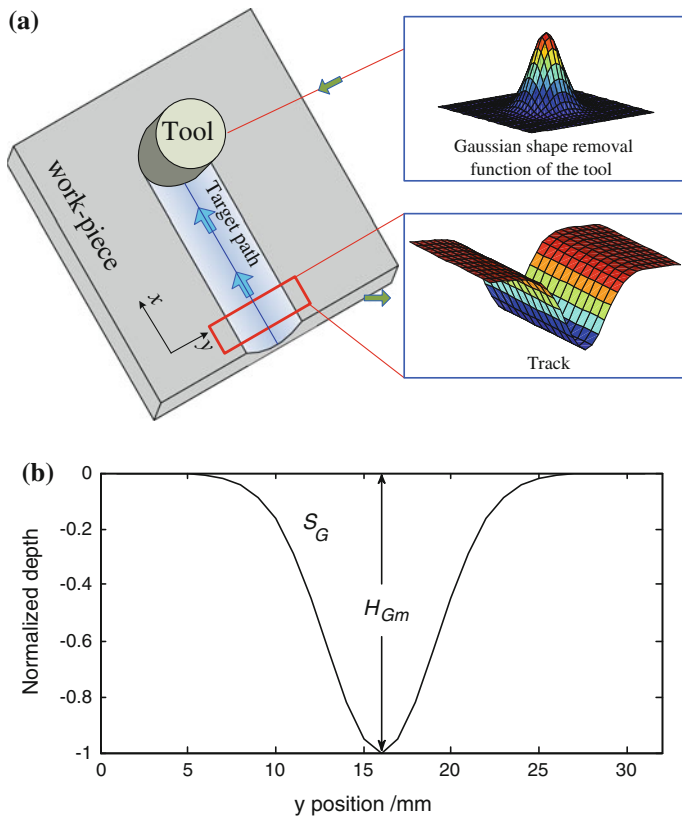


**Fig. 2.1** Effect of gaussian function. **a** Schematic view of the movement of the tool; **b** Cross section of the track along the y direction

maximum depth and the cross-sectional areas of material removal with a Gaussian removal function along the target orbit (in actual processing, the target orbit always includes regular orbit and complex orbit, e.g., scanning orbit, concentric-circles orbit, spiral orbit, peano-like orbit, and pseudo-random orbit).

Material removal is modeled by assuming that a tool with an URF moves along a certain orbit at a specific velocity. The movement velocity can be described as a function of the dwell time  $D(x, y)$ . Therefore, material removal depends on the URF and the dwell time on a certain part of the surface. This process can be presented by a two-dimensional convolution between the URF and the dwell time along a processing orbit.

$$\begin{aligned}
 E(x, y) &= R(x, y) * D(x, y) \\
 &= \iint_{\text{path}} R(x - x', y - y') \cdot D(x', y') dx' dy' \quad (2.3)
 \end{aligned}$$

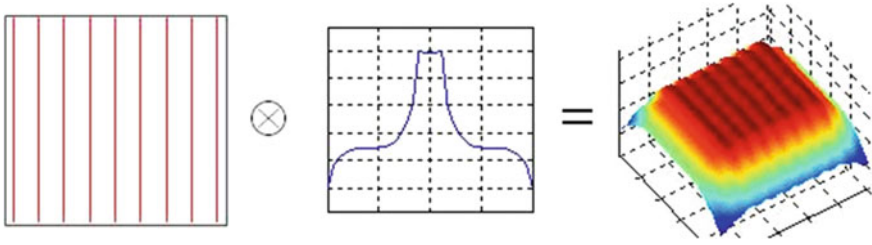


**Fig. 2.2** The diagram of discrete convolution of raster orbit and URF

where  $E(x, y)$  is the amount of removed material on the surface, and  $(x - x', y - y')$  is the transformational relation of coordinate systems between the removal function and the work-piece.

The dwell map and URF are complicated, which cannot be expressed by analytic function. A numerical method and mesh data were used to simulate the convolution model and visualize the orbit effect. The URF and dwell time map were both meshed into discrete points with same sampling intervals. The prescribed tool orbit was projected onto the dwell time map. Those points that were covered by projected orbit retained their primary value. Other points were set to zeros. The process is similar to draw orbits on screen with different color value, and some computer graphics algorithms, such as the digital differential analyzer and Bresenham algorithms, can be adapted directly to generate tool orbits on mesh data. Therefore, discrete convolution can be simulated with a new projected dwell map and discrete URF. Figure 2.2 shows the convolution results of a discontinued raster orbit and a typical orbit URF. The periodic distribution is obvious because of the effect of adjacent orbits.

The simulation precision and computation depends on sampling intervals mostly. When sampling intervals are small enough or the size of surface is large, the mesh data may become so large that the cost of computation can increase sharply. Another potential problem is that the real smooth orbit discretized on a mesh becomes discontinuous, even straight lines. Figure 2.3 shows a discretized but discontinuous smooth curve and straight line on a dwell map.

The traditional tool orbit distribution strategies include the spiral orbit (Fig. 2.4a), continuous or discontinuous raster orbit (Fig. 2.4b), contour orbit (Fig. 2.4c), and cubic B-spline curves. The amount of material removed from some points may differ from one another even if the same URF and space are used because these points are on different orbits. A tool orbit is usually composed of curves, lines, and corners. Their effects are examined in the next section.

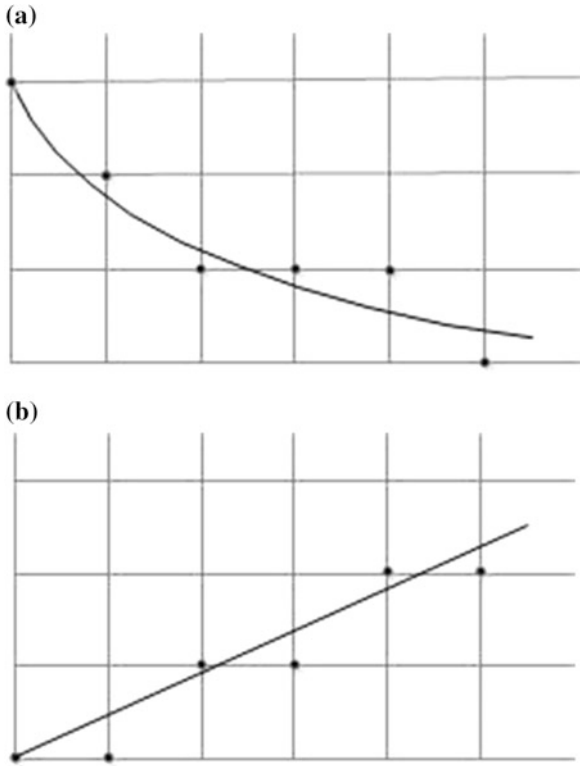


**Fig. 2.3** Discrete points of tool orbit on mesh. **a** Smooth curve; **b** straight line

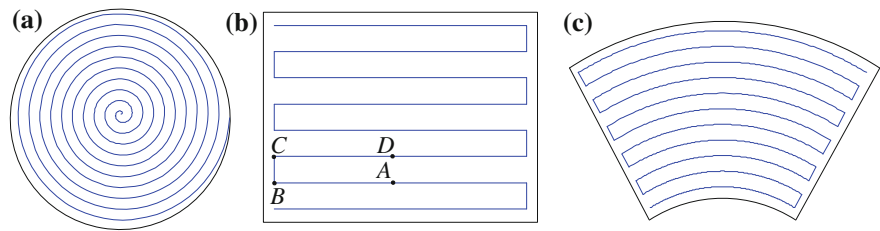


**Fig. 2.4** Traditional tool orbit distribution. **a** Spiral; **b** raster; **c** contour

## 2.2 Linear Orbit Features

### 2.2.1 Transformation Model of Gaussian Function

In fact, without eccentric rotation motion, the removal function in a normal press (i.e., small pad tool) or impact (i.e., fluid jetting tool) presents an annular distribution with a nearly M-shaped profile, which has a valley in the middle and two

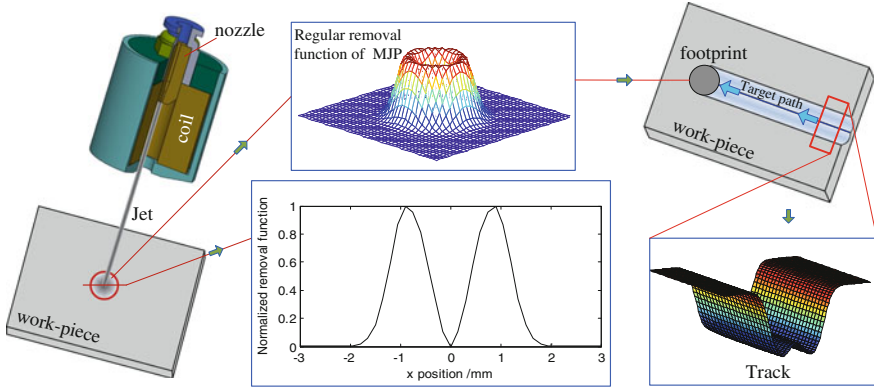


**Fig. 2.5** The regular removal function without eccentric rotation motion

symmetrical peaks at the adjacent margins (see Fig. 2.5, this regular removal function is obtained by using a cylindrical nozzle with 0.9 mm diameter, and the distance between the two peaks is about 1.4 mm). If this type of tool moves along an orbit (Fig. 2.1a), then the track has a degenerative W-shaped profile (two deep trenches with a shallow part in between).

To obtain the track as shown in Fig. 2.1, the M-shaped removal function should be changed into the Gaussian-like removal function. The common method is to take a tool rotating around the target point as shown in Fig. 2.6a. However, it is difficult to implement because of the complex mechanical and air-press or jet-liquid systems. Therefore, another way to optimize the orbit is presented and adopted. Instead of moving along the target orbit with Gaussian-like removal function, the regular tool-pad moves along two real orbits (see Fig. 2.6b) with appropriate line spacing. With this approach, the distribution of Gaussian removal function can be obtained. This optimized tool-orbit is called “multiplex line orbit”. Without loss of generality, the linear orbit is adopted as an example. Real orbits 1 and 2 are located on the opposite sides parallel to the target orbit (distance is  $dl$ ). Real orbits 1 and 2 form the multiplex orbit. For the linear orbit or the orbit with a large curvature radius, the distance between real orbit 1 and the target orbit is  $dl/2$ .

The different profiles (see Fig. 2.7a, b) and depths (see Fig. 2.7c) of the tracks can be obtained by adjusting the  $dl$  on the basis of the M-shaped removal function. Figure 2.7a shows that the profile has a U-shaped form for  $dl = 0.6$  mm. When  $dl$  increases, the profile will change from U-shaped form into V-shaped form. Specifically, the distribution of material removal is V-shaped for  $dl = 0.8$  mm (see Fig. 2.7b), which is similar to the distribution in Fig. 2.1. The profiles gradually change back into a U-shaped form, which is wider and shallower than the form with a smaller  $dl$ . In addition, the depth of the track does not depend linearly on  $dl$ . More removal materials are present along the target orbit for  $dl < 1.6$  mm. And the maximum depth gradually decreases as the  $dl$  increasing. Especially, for  $dl > 2.2$  mm, the maximum depth gradually flattens out with increasing  $dl$ . This

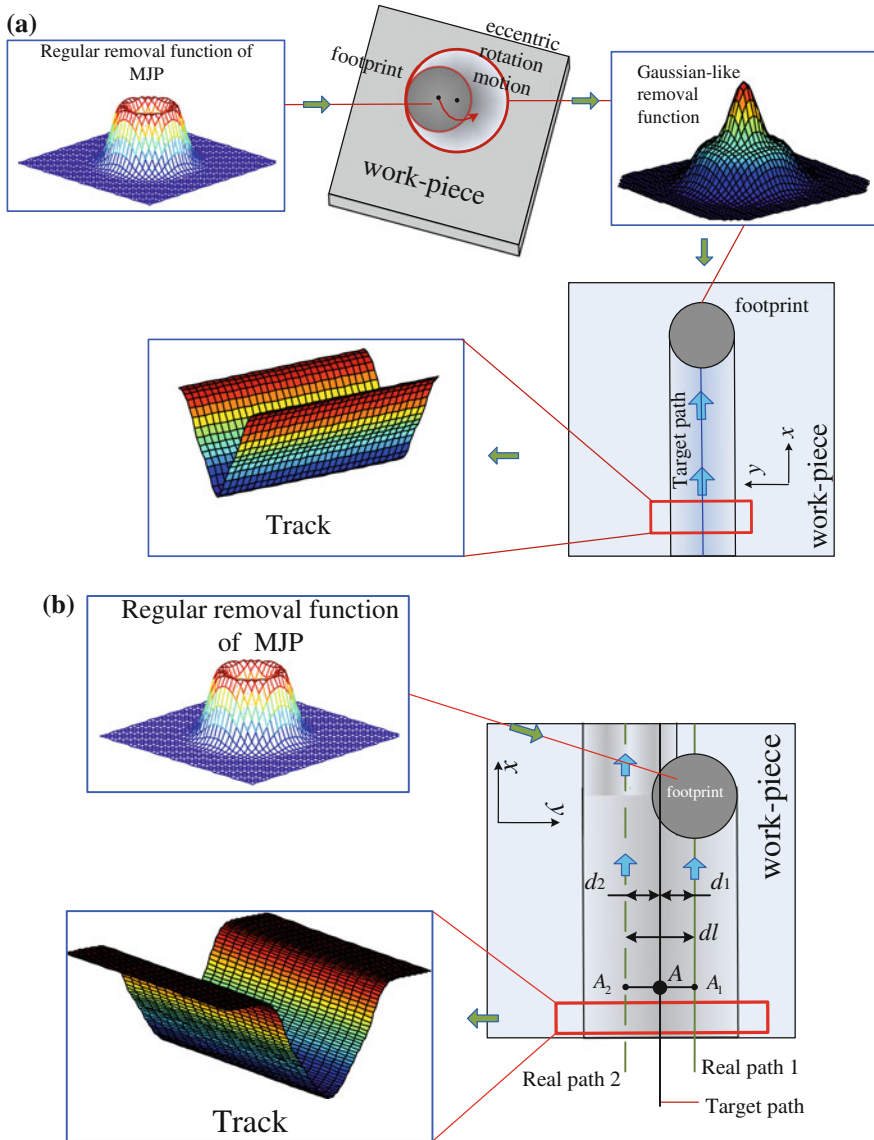
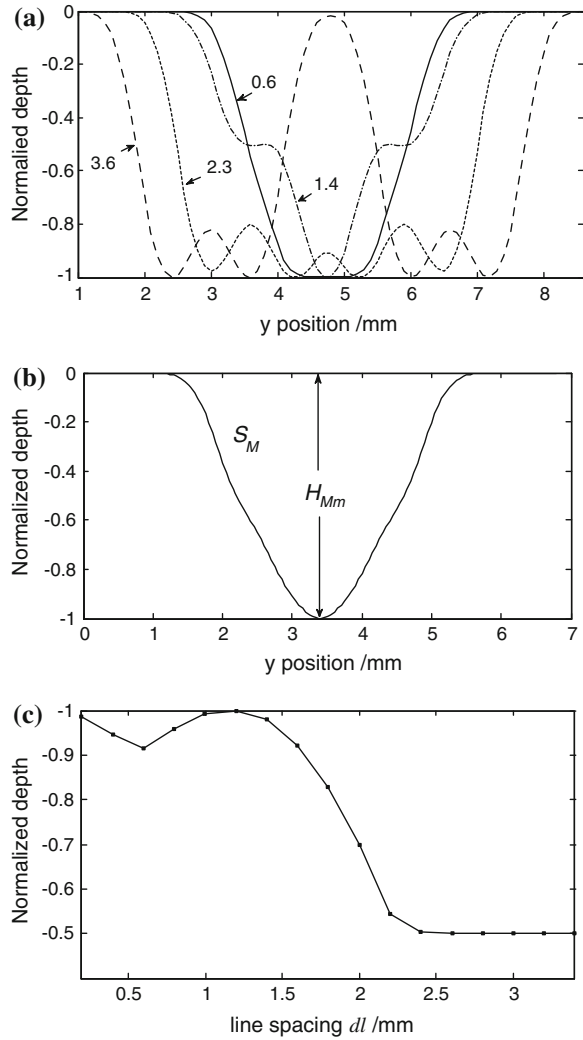


**Fig. 2.6** Methods to create V-shaped profile track by regular removal function. **a** Optimizing removal function; **b** using multiplex orbit

result is deceptive because the footprints begin to separate.  $H_{Mm}$  and  $S_M$  are, respectively, the maximum depth and the cross-sectional areas of material removal along the multiplex orbit (see Fig. 2.7b).

Therefore, for  $dl = 0.8$  mm, the track of the multiplex orbit for the M-shaped removal function is equivalent to that of the target orbit of the Gaussian removal

**Fig. 2.7** Effect of the *M-shaped* removal function after translation in the *x* direction along the multiplex orbit.  
**a** Cross sections of the tracks with different *dl* along *y*;  
**b** track profile for *dl* = 0.8 mm; **c** depth of the tracks with different *dl*



function. In line with this, the Gaussian removal function is the corresponding function of M-shaped one.

In mathematical modeling, to obtain the corresponding Gaussian shape from the M-shaped removal function, the profile parameters of the two distributions (see Figs. 2.1b and 2.7b) should satisfy the condition,

$$\begin{cases} H_{Gm} = H_{Mm} \\ S_G = S_M \end{cases}, \quad (2.4)$$



where  $H_{Gm}$ ,  $S_G$ ,  $H_{Mm}$ , and  $S_M$  are given as:

$$H_M(x_A, y) = \int_{RP_1} R_w(x_A - x'_1, y - y'_1) D_{w1}(x'_1, y'_1) dx'_1 \\ + \int_{RP_2} R_w(x_A - x'_2, y - y'_2) D_{w2}(x'_2, y'_2) dx'_2 \quad (2.5)$$

$$H_{Mm} = \max[H_M(x_A, y)] \quad (2.6)$$

$$S_M = \int H_M(x_A, y) dy \quad (2.7)$$

$$H_G(x_A, y) = \int_{\text{Path}} R_G(x_A - x', y - y') D_G(x', y') dx' \quad (2.8)$$

$$D_G(x_A, y_A) = D_{w1}(x_{A1}, y_{A1}) + D_{w2}(x_{A2}, y_{A2}) \quad (2.9)$$

$$H_{Gm} = \max[H_G(x_A, y)] \quad (2.10)$$

$$S_G = \int H_G(x_A, y) dy \quad (2.11)$$

where  $RP_1$  and  $RP_2$  are, respectively, the real orbits 1 and 2 on multiplex orbit, simultaneously,  $D_{w1}$  and  $D_{w2}$  are the dwell time function on the  $RP_1$  and  $RP_2$  with the M-shaped removal function  $R_w$ .  $D_G$  is the dwell time function on the target orbit with corresponding Gaussian function  $R_G$ . Especially, for the linear orbit or the orbit with a large curvature radius,  $D_{w1} = D_{w2} = D_G/2$ .

According to Eqs. (2.4) to (2.11), the  $\mathbf{B}$  and  $\mathbf{u}$  in Eq. (2.3) can be calculated to express the corresponding Gaussian removal function. If the tool-pad across point A (Fig. 2.6b) with constant velocity  $v$  along the orbit has large curvature radius,  $H_{Gm}$  and  $S_G$  can be described as:

$$\begin{cases} H_{Gm} = \max \left\{ \int B \cdot \exp[-u(x^2 + y^2)] \cdot T dx \right\} = TB \left( \frac{\pi}{u} \right)^{1/2} \\ S_G = \iint B \cdot \exp[-u(x^2 + y^2)] \cdot T dx dy = TB \frac{\pi}{u} \end{cases} \quad (2.12)$$

where  $T$  is the average time which is equals to  $2/v$ .  $\mathbf{B}$  and  $\mathbf{u}$  can be calculated on the basis of Eqs. (2.4) and (2.12).

$$\begin{cases} B = \frac{H_{Mm}^2}{S_M T} \\ u = \frac{H_{Mm}^2 \pi}{S_M^2} \end{cases} \quad (2.13)$$

### 2.2.2 The Processing Steps with Multiplex Orbit

Figure 2.8a shows a diagram of the optical finishing process applies the multiplex orbit. The surface error of the work-piece and the M-shaped removal function are measured by, e.g., an optical interferometer. The data for the initial surface error and

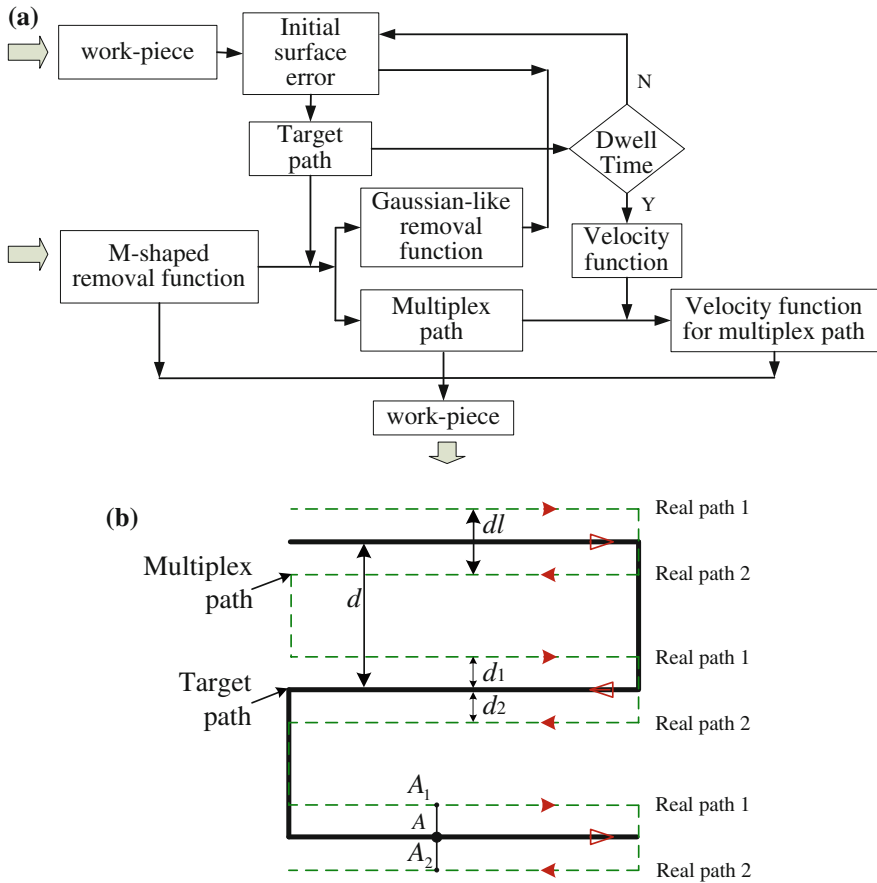


**Fig. 2.8** Processing steps with multiplex orbit. **a** Diagram of the simple simulation steps; **b** scanning orbit as an example

the M-shaped removal function are inputted to the computer. The appropriate target orbit is calculated (without loss of generality, the scanning orbit is adopted as an example in Fig. 2.8b,  $d$  is line spacing of the target orbit). The distribution of the material removal with V-shaped profile is obtained by adjusting the  $d/l$  through experiment or simulation. Therefore, the corresponding Gaussian removal function of the M-shaped removal function can be calculated through Eq. (2.4) by using  $H_{Mm}$  and  $S_M$ . The multiplex orbit is also simultaneously obtained (see Fig. 2.8b, which is formed by the real orbits. The dwell-time function on the target orbit is calculated by using the best-fit equations on the basis of the initial surface error, target orbit, and Gaussian removal function. The velocity on the target orbit, which is apt for computer numerical control, can be established by this dwell-time function. The corresponding velocity on the multiplex orbit is computed by using the velocity of the target orbit via Eq. (2.9). A finishing program is then implemented on the work-piece with M-shaped removal function, multiplex orbit, and corresponding velocity function.

It is obvious to see that the Gaussian removal function and target orbit are easily applied to calculate the parameters for finishing in the simulation step. The M-shaped removal function and multiplex orbit are more feasible in the actual finishing step, as they not only retain the advantages of Gaussian removal function for precise finishing, but also easy to implement in actual processing.

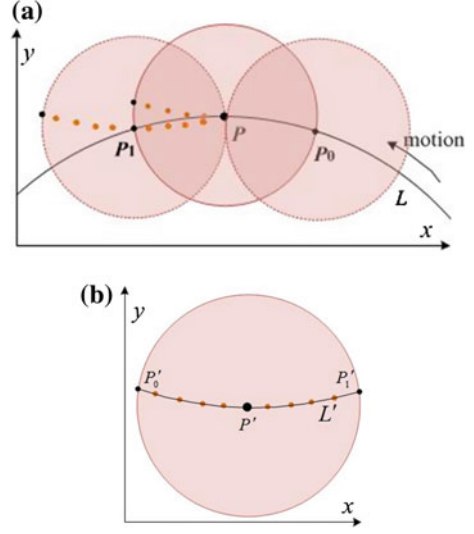
Changing the M-shaped removal function into a Gaussian-like removal function is complicated, e.g., in fluid jetting finishing process, the eccentric rotation motion for nozzle and coil, transmitting a steady current and slurry form of static system to the coil and nozzle, and designing and implementing gesture and position for fixing the nozzle. Thus, the regular M-shaped removal function is applied for actual processing, which is simpler than the above-mentioned approaches.

## 2.3 Curve Orbit Features

In simulations, tool orbits can generally be considered from two directions: along the orbit and normal to the orbit. Numerous studies have been reported about the direction of normal to the orbit in literatures. The space between adjacent orbits is the key parameter that affects final surface quality. In the section, a mathematic model was put forward to present the effects of the curvatures and corners along an orbit during finishing. Actually, the URF may cover several orbits, which depends on the space between adjacent orbits.

When URF moves along orbit  $L$  and stays on every point of the orbit, the removal amount of point  $P$  is the accumulations of removal amount of adjacent point on curve from  $P_0$  to  $P_1$  (Fig. 2.9a). The relative position of  $P$  in every URF, which lies on different point on curve  $\widehat{P_0P_1}$ , forms a curve  $L'$  (shown in Fig. 2.9b). Curve  $L'$  is opposite with Curve  $L$  in up-down and left-right directions. Then, the accumulations of  $P$  can become the integral over curve  $L'$ ,  $P'$ ,  $P'_0$ , and  $P'_1$  are the points relative to point  $P$  when the URF lies on  $P$ ,  $P_0$ , and  $P_1$ .

**Fig. 2.9** The diagram of mathematic model along orbit (pink filled circle denote as the URF). **a** The URF moves through point  $P$ ; **b** the relative position of point  $P$  forms curve  $L'$  when the URF lies on all points in curve  $L$



If the URF is of rotational symmetry, actually most URFs of finishing tools are rotational symmetry, or the orbit is symmetrical, the amount of removed material is equal to the integral along orbit  $L$  instead of  $L'$ . Assuming that the URF can be expressed as  $g(x, y)$ , the dwell map is denoted as  $f(x, y)$ , the amount of material removed of point  $p(x, y)$  in curve  $L$  can be written as:

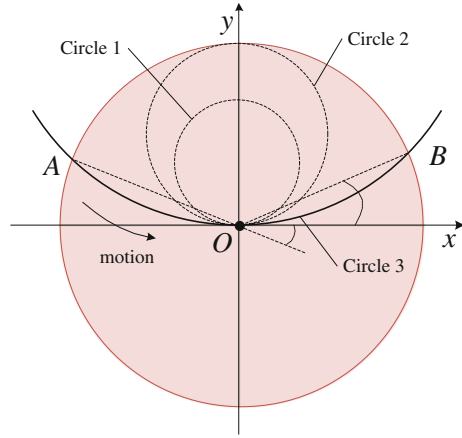
$$d(x, y) = \int_L f(x, y)g(x, y)ds = \lim_{\lambda \rightarrow 0} \sum_{i=1}^n f(\xi_i, \eta_i)g(\xi_i, \eta_i)\Delta s_i \quad (2.14)$$

Curve  $L$  was divided into  $n$  segments,  $(\xi_i, \eta_i)$  is the value of the  $i$ -th point,  $\Delta s_i$  is the arc-length of the  $i$ -th segment, and  $\lambda$  is the maximum arc-length of segments. The removal amount can be regarded as the weighted arc-length covered by the URF, and the weight of every point depends on the value of  $f(\xi_i, \eta_i)g(\xi_i, \eta_i)$ . For constant finishing, the weight depends on  $g(\xi_i, \eta_i)$ , and the length covered by the URF can describe the trend of removal amount along an orbit to a certain extent.

### 2.3.1 Effects of Curvatures

When the URF passes through a point via different orbits with different curvature, the removal amount may differ with each other. Then, a series of circle orbits with different curvatures were built and passed through the center of the URF, as shown in Fig. 2.10. The circle orbits with various curvatures are expressed as  $r = 2a \sin \theta$  in polar coordinates, where  $a$  is the radius of the circle. The circle orbit in Cartesian coordinates can be expressed as:

**Fig. 2.10** Diagram of different curvature orbits (*pink filled circle* denote as the URF)



$$\begin{cases} x = \varphi(\theta) = r \cos \theta = 2a \cos^2 \theta \\ y = \psi(\theta) = r \sin \theta = 2a \cos \theta \sin \theta \end{cases} \quad (2.15)$$

According to Eq. (2.14), the amount of material removed from point  $O$  can be calculated as follows:

$$d(x, y) = \int_{\beta}^{\alpha} g[\varphi(\theta), \psi(\theta)] \sqrt{\varphi'^2(\theta) + \psi'^2(\theta)} d\theta \quad (2.16)$$

where  $\alpha$  and  $\beta$  are the coordinate of points  $A$  and  $B$ .

If  $0 < a \leq 0.5$ ,  $\alpha = -0.5\pi$ ,  $\beta = 0.5\pi$ , and if  $a > 0.5$ ,  $\alpha = -\arcsin 1/2a$ ,  $\beta = \arcsin 1/2a$ . On the basis of circle orbit symmetry, Eq. (2.16) can be simplified as:

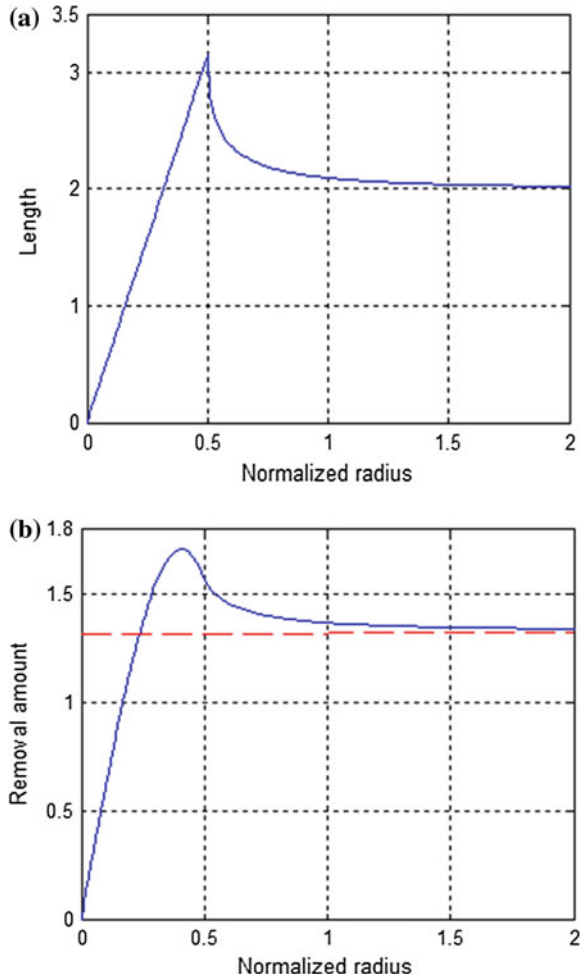
$$\begin{aligned} d(x, y) &= 2 \int_0^{\alpha} g[\varphi(\theta), \psi(\theta)] \sqrt{\varphi'^2(\theta) + \psi'^2(\theta)} d\theta \\ &= 4a \int_0^{\alpha} g(r) d\theta \end{aligned} \quad (2.17)$$

Assuming  $g(x, y)$  is equal to 1 mathematically, although it does not exist physically. The signification of  $d(x, y)$  became the length covered by the URF, and can be expressed as,

$$l = \begin{cases} 2\pi a, & a \leq 0.5 \\ 4a \arcsin\left(\frac{1}{2a}\right), & a > 0.5 \end{cases} \quad (2.18)$$

When the URF moves along the circle orbit, a numerical method was used to calculate the Eqs. (2.17) and (2.18). The curvature of the circle orbit was normalized with respect to the URF radius. Figure 2.11 shows the results of the length covered by the URF and removal amount along the circle orbit. Generally, the trend of the length curve is similar to that of the removal amount curve. The length and the removal amount increase rapidly before reaching their maximum values, then decreases exponentially and approaches to 2 or  $h_{\text{line}}$  over the peak. The peak of the

**Fig. 2.11** Curves of **a** length covered by the URF and **b** removal amount as a function of radius of curvature



length curve appears at 0.5, whereas that of the removal amount curve appears at 0.41 because the weight of the URF is not greater than 1.

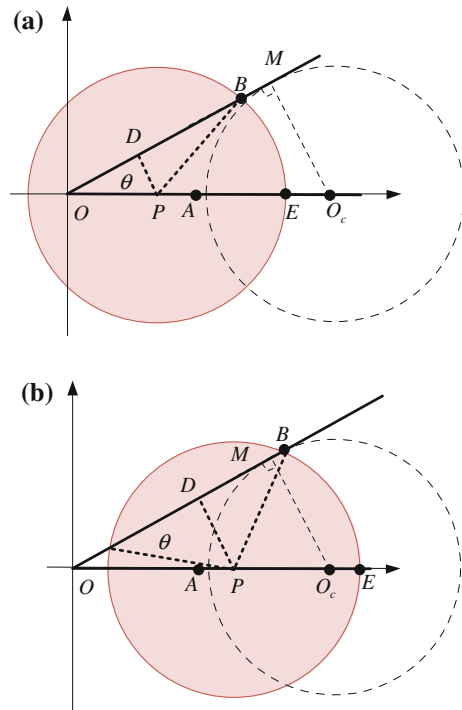
The curves of the length and removal amount indicate that a small radius of curvature may cause additional material removal. Because the removal amount along orbit can be considered as the weighted length covered by the URF, the length curve can predict the peak removal amount and its location to a certain extent.

### 2.3.2 Effects of Corners with Different Angles

Figure 2.12 shows the diagram of the URF moves toward a corner. When the center  $P$  of the URF lies on different position near the corner, the removal amount may differ because of the angle of the corner. In Fig. 2.12, the coordinate of point  $A$  is  $(1, 0)$  and that of  $P$  is  $(x, 0)$ . When the outline of the URF (dashed circle) is tangent to  $\overline{OM}$ , the center is  $O_c(1/\sin \theta, 0)$ .

According to the same method used for analyzing curvature mentioned above, the orbit near the corner can be divided into two segments expressed as Eq. (2.19), assuming  $\theta$  is an acute angle ( $\theta < 90^\circ$ ).

**Fig. 2.12** The URF moves toward a corner when its center  $P$  lies on **a**  $0 < x < 1$ ; **b**  $1 < x < 1/\sin \theta$



$$\begin{cases} y_{OE} = 0 \\ y_{OB} = x \tan \theta \end{cases} \quad (2.19)$$

The length covered by the URF was considered first. The following conditions depend on the value of point  $P$ : (1)  $x > 1/\sin \theta$ , which is degraded to a line orbit; (2)  $1 < x < 1/\sin \theta$  (Fig. 2.12b); (3)  $0 < x < 1$  (Fig. 2.12a); (4)  $x < 0$ , which is an invalid condition. On the basis of geometric relationships, the orbit length covered by the URF can be written as

$$l = \begin{cases} x + x \cos \theta + \sqrt{1 - x^2 \sin^2 \theta} + 1, & 0 \leq x < 1 \\ 2\sqrt{1 - x^2 \sin^2 \theta} + 2, & 1 \leq x < 1/\sin \theta \\ 2, & x \geq 1/\sin \theta \end{cases} \quad (2.20)$$

If  $\theta > 90^\circ$ , the length can be written as

$$l = \begin{cases} x + x \cos \theta + \sqrt{1 - x^2 \sin^2 \theta} + 1, & 0 \leq x < 1 \\ x \geq 1 \end{cases} \quad (2.21)$$

Figure 2.13 shows the simulation of the removal amount, when the URF moves along a corner with a  $60^\circ$  angle. The blue solid curve shows the removal amount, and the red solid curve is the corner orbit in the X–Y plane. The removal amount approaches to  $h_{\text{line}}$ , when the URF moves away from the corner. Two peaks appear at points (0.568, 0) and (0.284, 0.492) near the corner. The distances of the two peaks to the corner are very similar ( $0.284^2 + 0.492^2 \approx 0.568^2$ ).

Figure 2.14 shows the curves of length covered by the URF and removal amount with different angle. They have the same trend. Near the corner, both of them initially increase with angle decreases, then declines to a certain limit. Away from the corner, they approach to constant (2 or  $h_{\text{line}}$ ). When the angle nears  $180^\circ$ , the curve of removal amount is close to a line.

**Fig. 2.13** Curve of removal amount along a corner with  $60^\circ$  angle

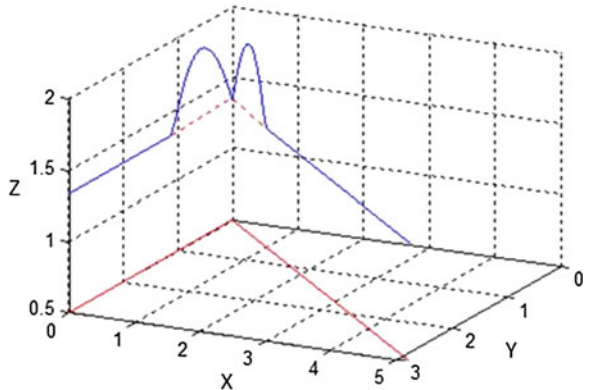
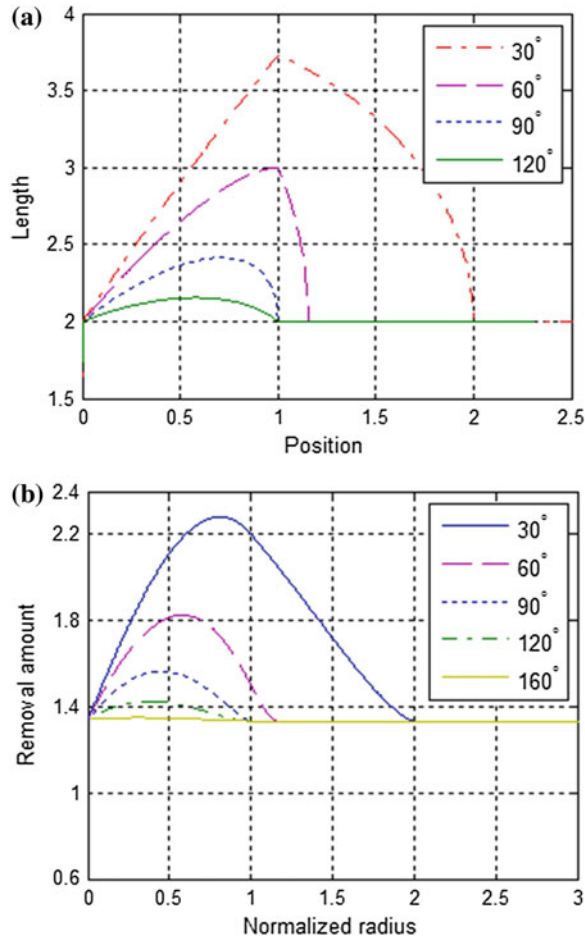




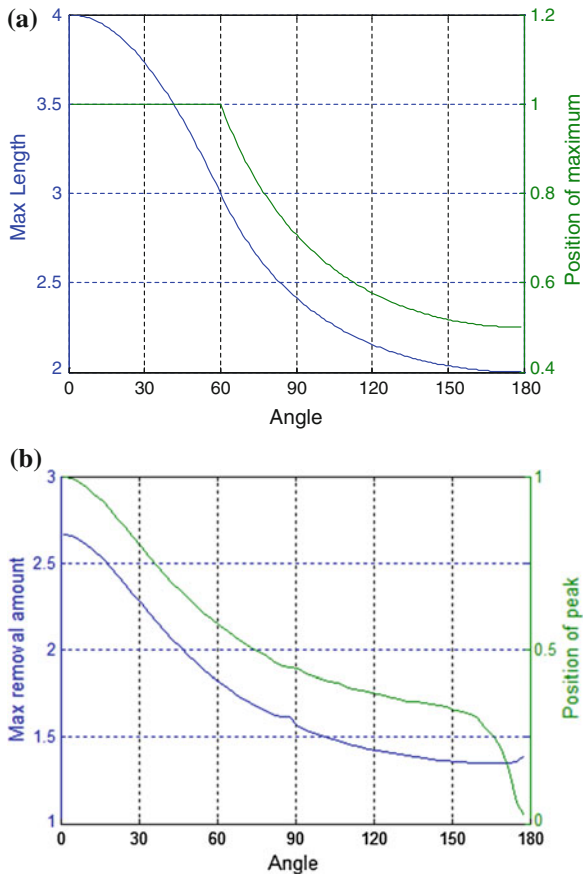
**Fig. 2.14** The curves of **a** length covered by URF and **b** removal amount as a function of position



Furthermore, all peaks of the curves of removal amount and length with different angles were calculated and shown in Fig. 2.15. The maximal length decreases from 4 to 2 with increasing angle, and its position decreases from 1 to 0.5. The position of the peak is equal to 1 at an angle of less than 60°. The maximal removal amount curve decreases from  $2h_{\text{line}}$  to  $h_{\text{line}}$  with increasing angle, and its position decreases from 1 to 0. Both have the similar trend, and the maximal removal amount and its position can be predicted through that of length curves.

According to Fig. 2.13, more materials were removed around the corner. The additional peaks will affect the removal map of the surface. It is beneficial to obtain the corner distribution of the tool orbit before finishing. Typical corner detection algorithms, such as Harris algorithm can be used to detect the corner distribution of orbit and predict the removal map. Figure 2.16 shows a type of Peano orbit, and its

**Fig. 2.15** Curves of  
**a** maximum length and  
**b** maximum removal amount



corner detection by using of the Harris algorithm. The corner of the Peano orbit is well distributed, in which the removal map may contain well distributed peaks and a good surface texture.

## 2.4 Combined Effect

The effects of curvatures and corners along an orbit were discussed in the preceding sections. To a certain extent, the removal amount curve and its position are proportional to the length curve. Actually, the removal amount is a combined effect of corners, curvatures, and adjacent orbits. In this section, two typical orbits, spiral and raster orbits were discussed.

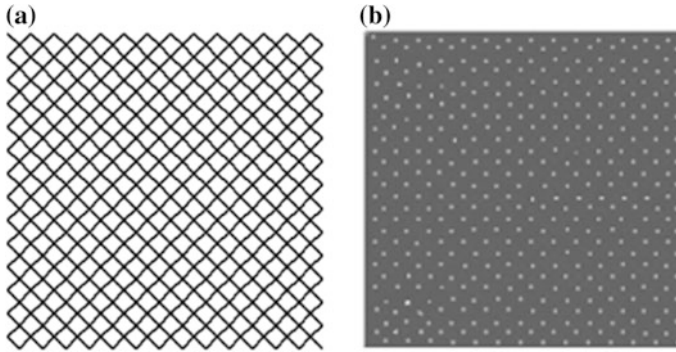


**Fig. 2.16** The diagram of **a** Peano orbit and **b** its corner detected result

### 2.4.1 Spiral Orbit

Spiral orbit is a common trajectory for finishing circular optical components, which can be expressed as  $r = a + b\theta$  in polar coordinates. Equation (2.22) is expressed in Cartesian coordinates. In this equation,  $a$  and  $b$  are constants. The space between successive turnings is  $2\pi b$ . The curvature decreases with increasing  $\theta$ , and the removal amount may change because of the curvature.

$$\begin{cases} x = \varphi(\theta) = (a + b\theta) \cos \theta \\ y = \psi(\theta) = (a + b\theta) \sin \theta \end{cases} \quad (2.22)$$

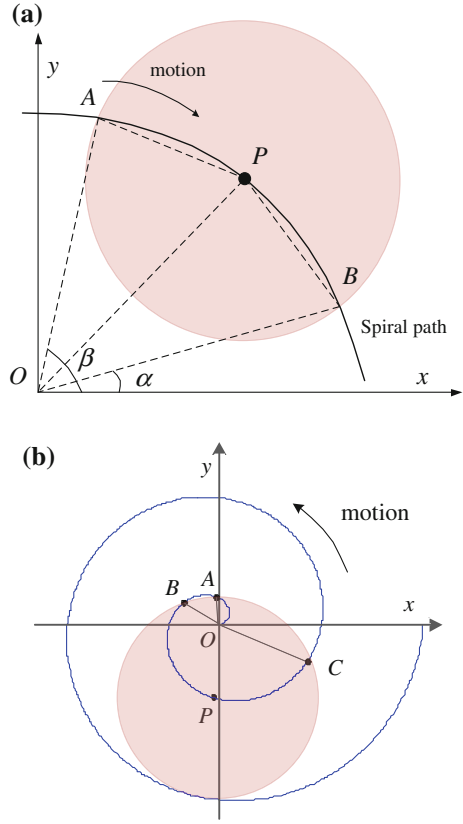
The amount of material removed from any point in a spiral orbit can be calculated according to Eq. (2.23),

$$d(x, y) = \int_{\alpha}^{\beta} g(r) \cdot \sqrt{(a + b\theta)^2 + b^2} d\theta \quad (2.23)$$

where  $\alpha$  and  $\beta$  are the azimuths of intersections (Fig. 2.17a). Assume that the distance between successive turnings is equal to the radius of the URF, and the URF lies on point  $P(r, \theta)$  in polar coordinates. If  $P(r, \theta)$  is far from the origin, angles  $\alpha$  and  $\beta$  can be easily solved using the cosine law,  $\cos(\theta - \alpha) = (r^2 + (b\alpha)^2 - 1)/(2br\alpha)$ . If  $r \gg 1$ ,  $\cos(\theta - \alpha) \approx 1/r$ . The cosine equation becomes a unary quadratic equation, which is easy to solve.

If point  $P$  is near the origin, the situation becomes complicated (as shown in Fig. 2.17b). The URF covers  $\widehat{OA}$  and  $\widehat{BC}$  segments. Equation (2.23) becomes the integration over  $\widehat{OA}$  and  $\widehat{BC}$ , and all the limits of integration of each segment should be individually solved. Because it is difficult to obtain an exact solution, numerical method can be used to calculate the approximate solution of all limits and the integral.

**Fig. 2.17** The URF covered spiral orbit when center point  $P$  **a** far away from the origin  $O$  and **b** near the origin  $O$

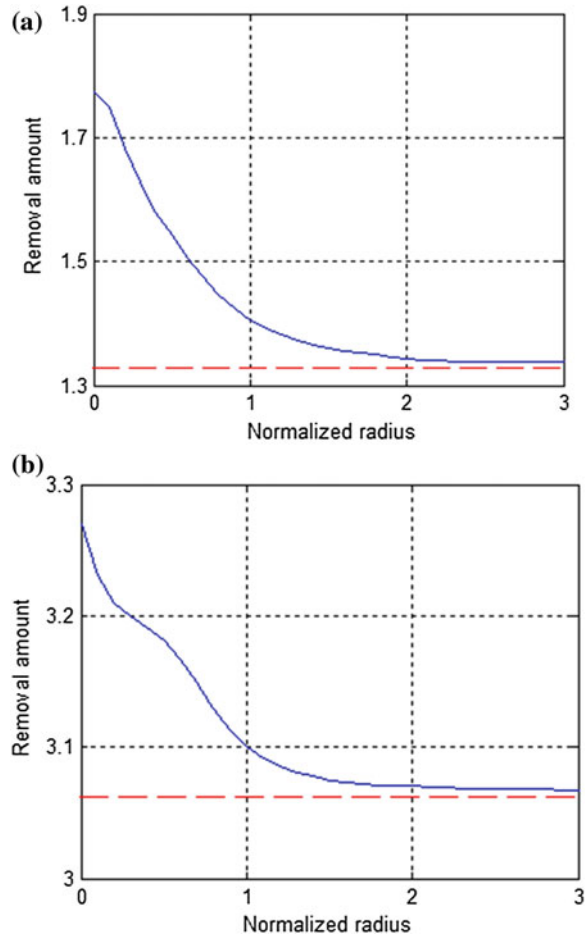


By the same method, when the URF center point  $P$  is far from the origin, let  $a = 0$ , the arc-length cover by the URF can be expressed as:

$$l(r, \theta) = \int_{\alpha}^{\beta} b \sqrt{1 + \theta^2} d\theta = \frac{b\theta}{2} \sqrt{1 + \theta^2} + \frac{b}{2} \ln(\theta + \sqrt{1 + \theta^2}) \Big|_{\alpha}^{\beta} \quad (2.24)$$

The removed amount of any point can be calculated by considering the weight of the URF. These points along the arbitrary radius were chosen for simulation because of rotational symmetry. The amount of removal is equal to the effect of the curvature when the space between successive turnings is greater than 1. Figure 2.18 shows the removal amount curve with different spaces. A peak exists in the center of the spiral orbit. The amount of removal decreases and approaches a limit (normalized radius greater than 2) with increasing normalized radius. The peak diameter is about four times of the normalized radius. The ratio between the peak value and the limit of space = 1 is approximately  $1.77/1.34 \approx 1.3$ .

**Fig. 2.18** The arc-length and removal amount curve with different space. **a** Space = 1; **b** space = 0.5



### 2.4.2 Raster Orbit

Raster orbit is another popular trajectory for rectangular optical elements. Because of periodicity, only one periodic orbit is considered, orbit  $ABCD$  as shown in Fig. 2.4b. In the middle of raster orbit, the removal characteristics are similar to the line orbit. Around the turning points on edges (point  $B$  and  $C$ ), the corner and adjacent orbits will affect the removal amount. 3D curves of removal amount were shown in Fig. 2.19 with different spaces between adjacent parallel lines. The space has been normalized with respect to the URF radius. Red solid lines are the edge of raster orbit in the X–Y plane.

Because of the accumulation of adjacent orbits, the curve of removal amount along every periodic orbit is different with the effect of corner with  $90^\circ$  angle. All peaks appear around the turning point  $B$  and  $C$  (as shown in Fig. 2.19a), and the

distances to the corner are between 0.5 and 1. When the space is greater than 1, there are more than three peaks around the turning points, two peaks are on lines  $AB$  and  $CD$ , respectively, and others lie on edge  $BC$ . When the space is less than 1, the peaks become obscure with decreasing space. Both curves in line  $AB$  or  $CD$  approach a limit when the URF moves away from turning points. The ratio between the peak and the limit shows the smoothness of the curve, which is about 1.2 for a space equal to 1, and declines to about 1.04 when the space is equal to 0.5.

## 2.5 Process Validation

### 2.5.1 *Spiral Orbit Finishing*

Spiral orbit shown in Fig. 2.4a was adopted to finish a K9 mirror with 50 mm diameter. Specified parameters were chosen to produce a constant finishing. The diameter of the URF is about 8 mm, and the space between the successive turnings of the spiral orbit is about 4 mm.

The removal map (Fig. 2.20c) can be measured directly through subtracting the initial figure map (Fig. 2.20a) from the figure map after finishing (Fig. 2.20b) by a Zygo GPI interferometer. The removal depths at the edge of the surface differs, because the distance between the last turn of the spiral orbit and the edge of the surface is different. Thus, a scanning profile through the central point of the mirror was extracted and shown in Fig. 2.20d. An over finished area exists in the center of the mirror surface, as predicted in the last section. The width of the central area is about 16 mm (four times of the radius), which is consistent with the simulation results. The depth of the peak removal in the center is about 207.7 nm, the average removal depth is about  $207.7 - 73 = 134.7$  nm, and the ratio between them is about  $207.7/134.7 \approx 1.5$ . This result is slightly greater than the predicted value, because some materials at the edge of the mirror were removed. Nevertheless, this value confirms the validity of the model.

### 2.5.2 *Optimized Spiral Orbit*

The spiral orbit is normally planned in a two-dimensional (2D) surface map, and then projected onto the aspheric surface to generate a three-dimensional (3D) orbit. Although the pitch of the 2D orbit is an optimal constant, the pitch of the 3D orbit may vary depending on the local curvature of the optical element, especially for an aspheric surface with changing curvature. Figure 2.21 shows an ideal 2D spiral orbit with  $d$  as its pitch. During finishing, the removal function moves along the normal direction every time, and the actual pitch is  $d'$ . Furthermore,  $d'$  changes with

**Fig. 2.19** The removal amount curves of raster orbit.  
**a** Space = 1.5; **b** space = 1;  
**c** space = 0.8; **d** space = 0.5

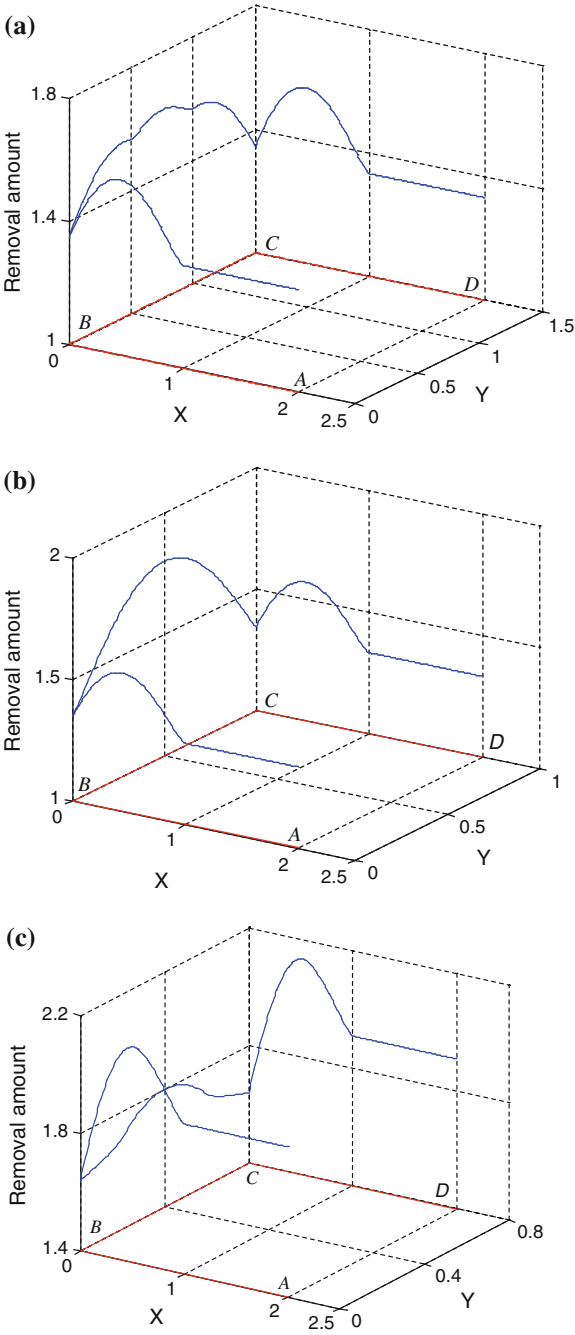
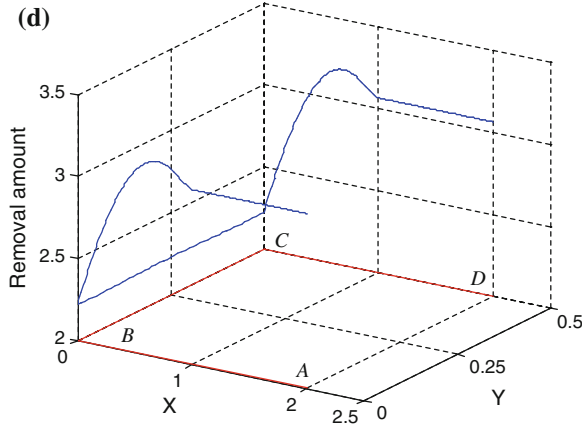


Fig. 2.19 continued



the coordinates, which may cause ripple errors. The spatial frequency is approximately  $1/\bar{d}'$ , where  $\bar{d}'$  is the average pitch.

This condition also occurs on other orbits such as the raster and fractal orbits. The changing pitch also affects the removal map. The peak-to-valley (PV) of the removal map is a function of pitch. The major trend is that PV decreases with the pitch. An extra simulation was proposed, and the results show that different shape removal functions have similar trends (Fig. 2.22), but the position of PV of the undulating curve is different.

The deviation from the desired pitch of the spiral orbit may affect the PV and the root-mean-square (RMS) of the removal map, and even cause some ripple errors. The difficulty is how to obtain all points of the spiral orbit and ensure that the distance between adjacent turnings is equal to the desired pitch. An iterative method was proposed to calculate the succeeding point based on a given start point (Fig. 2.23).

The calculation process is as follows:

- (1) Point  $P_0$  is assumed as the starting point, and the desired pitch is  $p$ .
- (2) To calculate the tangent ( $\overline{PN}$ ) of  $P_0$ , and obtain the angle  $\alpha_0$  between  $\overline{PN}$  and x-axis.
- (3) The  $x$  coordinate of the next point is obtained as  $x_1 = x_0 + p \cos \alpha_0$ . The intersection point  $P_1$  on the aspheric surface is calculated with the same  $x$ -axis coordinates as  $x_1$ .
- (4) The distance ( $p_1$ ) between points  $P_1$  and  $P_0$  can be calculated.
- (5) The difference between  $p_1$  and the desired pitch is obtained using the equation  $d_1 = \overline{P_0P_1} - p_1$ . Then, the angle  $\alpha_1$  between  $\overline{P_0P_1}$  and  $x$ -axis is determined.
- (6) Repeat steps (3)–(5) until the difference  $d_n$  is small enough, i.e.,  $d_n < \varepsilon$ , where  $\varepsilon$  is a small preassigned tolerance, whose value depends on the accuracy required.



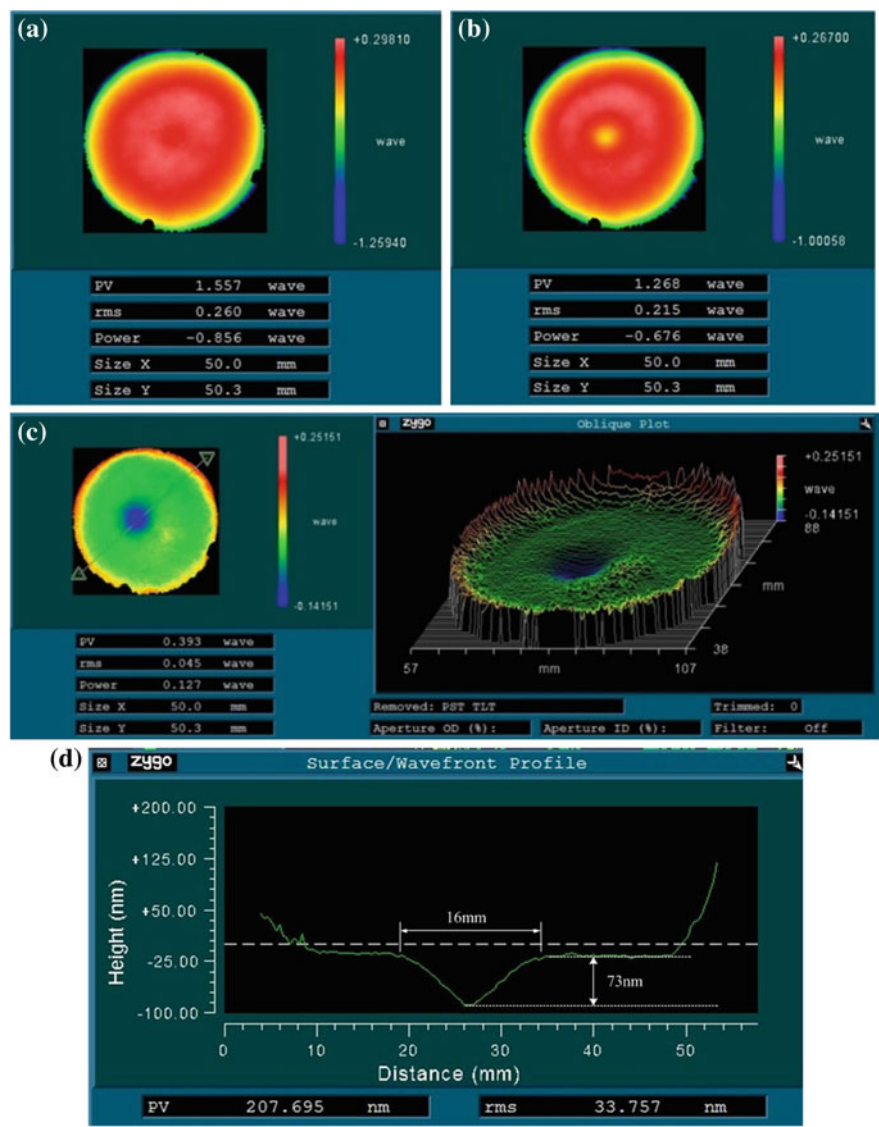


**Fig. 2.20** Process experimental results using spiral orbit. **a** Initial figure map; **b** figure map after finishing; **c** removal map; **d** the profile through the center point

(7) Assuming that  $P_n$  is the starting point, steps (2) and (6) are repeated, a serial point can be calculated.

An aspheric surface was chosen to verify the iterative method and can be expressed as Eq. (2.25):

**Fig. 2.21** Spiral orbit and its projection onto the aspherical surface

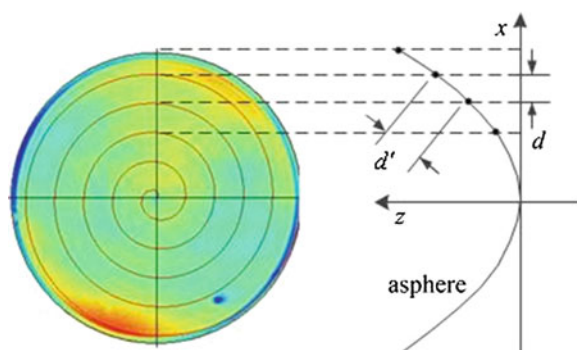


**Fig. 2.22** Peak-to-valley as a function of pitch. **a** Result with ellipse removal function; **b** result with the axisymmetric removal function

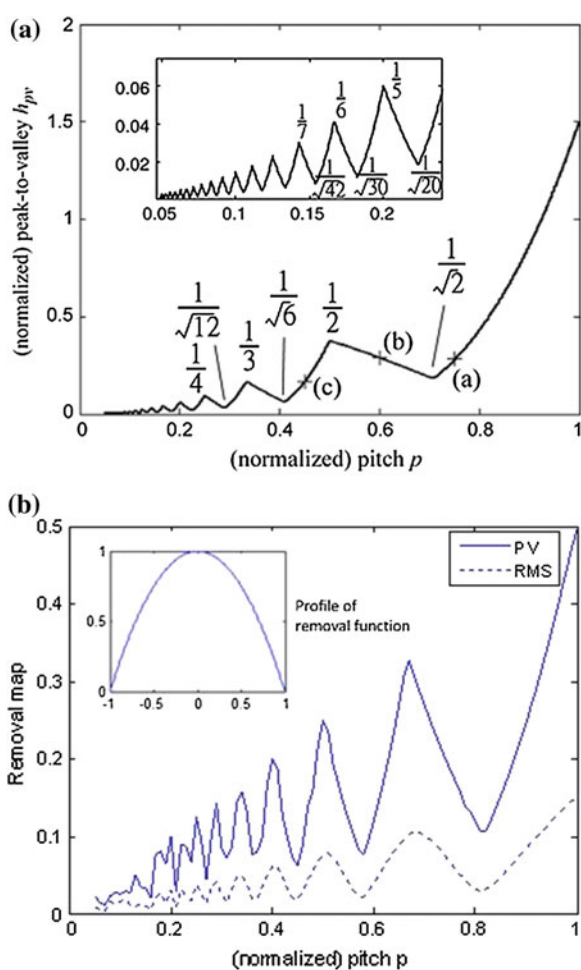
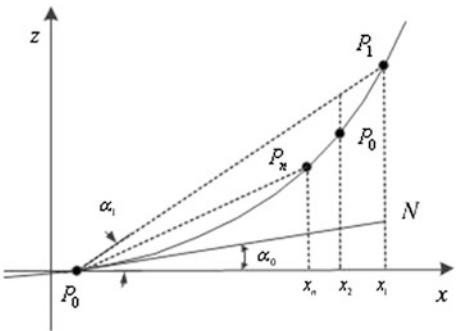


**Fig. 2.23** Diagram of iterative method



$$z = f(x, y) = \frac{cr^2}{1 + \sqrt{1 - (k + 1)c^2r^2}} + A_jr^{2j} + \dots \tag{2.25}$$

where  $c$  is the curvature of the vertex,  $k$  is the conic constant,  $r$  is the distance of curvature, and  $A_j$  is the constant of high order aspherics,  $j = 2, 3, \dots$

The radius of curvature is 500 mm, and the conic is  $-1$ , with the 4th order term  $A_2 = 1 \times 10^{-8}$ . The desired pitch is 5 mm, and the starting point  $P_0$  is (1, 0.001). The pre-assigned tolerance  $\varepsilon$  is 0.001 mm. The first 11 points were calculated and listed in Table 2.1. The results suggest that the method is highly accurate. According to actual computation, the precision after two iterations can almost meet the demands. For some low-gradient surfaces, a single iteration can already meet the demands.

**Table 2.1** Results from the iterative method

x/mm	z/mm	d <sub>n</sub> /mm	Iteration no.
1	0.001	—	—
5.99999	0.036013	0.000113	1
10.99998	0.121146	0.000715	1
15.99814	0.256596	0	2
20.99468	0.442719	-0.000001	2
25.98904	0.679992	-0.000001	2
30.98068	0.969015	-0.000003	2
35.969	1.310507	-0.000004	2
40.95338	1.705309	-0.000007	2
45.93317	2.154371	-0.00001	2
50.90765	2.658752	-0.000015	2
⋮	⋮	⋮	⋮

Adopting the aforementioned method, the 3D spiral orbit can be generated. The circumference is divided into  $N$  segments. Normally,  $N = 90, 180, 360 \dots$ . The points in the first turn can be calculated from the center point  $(0, 0)$ , and the desired distance to center is represented by  $i \cdot p/N$ ,  $i = 1, 2 \dots N$ . The point in the second turn can be obtained from the point in the first turn with the same angle, where the desired distance is the desired pitch ( $p$ ). Then, the method is applied to the 3rd, 4th... turn successively. Figure 2.24 shows a 3D spiral orbit for the aspheric surface using the iterative method. The space length between adjacent circles is equal, but the pitch in the X–Y plane decreases.

An axisymmetric paraboloid with a circular aperture of 600 mm was utilized. The radius of curvature of the vertex is 4,800 mm, and the conic is  $-1$ . A null compensator was designed by Zemax software, the designed data is shown in Table 2.2.

The initial surface error map is shown in Fig. 2.25a. Computer control finishing technology and all optimal strategies mentioned above were adopted. During finishing, 3D spiral orbits were generated for the aspheric surface using the iterative method. The pitch and removal function depend on the measured surface errors, which were corrected in every cycle of finishing. After five iterations, the surface error meets the demands as shown in Fig. 2.25b. The final distorted surface error was corrected. By way of the power-spectral-density (PSD) method, the average PSD curve result was calculated, and there is no obvious peak at spatial frequency  $1/5$  mm as shown in Fig. 2.25c.

**Fig. 2.24** 3D spiral orbit for aspheric surface. **a** Isometric view; **b** top view

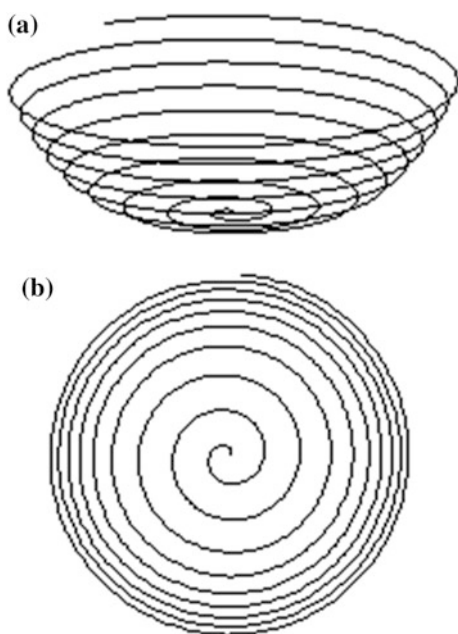


**Table 2.2** Design data of a null compensator

No.	Radius	Thickness	Index of glass	Semi-diameter
1	205.70	25	1.51	50
2	Infinity	266.94	—	50
3	−93.29	12.0	1.51	25
4	−318.10	5001.75	—	28

### 2.5.3 Raster Orbit Finishing

Raster orbit shown in Fig. 2.4b was adopted to perform finishing experiments. The space between the adjacent orbit lines is 4 mm. The URF adopted is same as that used in spiral orbit finishing. The removal map can be obtained by the same way as spiral orbit finishing (Fig. 2.26a). The area occupied by the raster orbit is about  $28 \times 28$  mm, and the area of the removal map is about  $36 \times 36$  mm. Each side is extended to about one radius of the URF because of the convolution effect. Figure 2.26b shows a profile (1) along the edge of the raster orbit (line *BC* shown in Fig. 2.4b) and another profile (2) along an inner line orbit (line *AB* direction in Fig. 2.4b). The lower left and lower right corners are the start and end points of the raster orbit, respectively. The location of the raster orbit can be easily determined. Thus, profile (1) and profile (2) were selected from the removal map.

The undulate profile (1) suggests the periodicity of the raster orbit with a period of approximately 8 mm (two times of the space between the adjacent lines). Profile (2) shows that two peaks appear at the left and right sides of the profile, and the distant of each peak to the side is about 6 mm, which is consistent with the prediction results of the model. The ratio between the maximum and average removal depths is  $137/125 \approx 1.1$ , which approximates the simulation result. Notably, the valley of profile (1) is lower than the average removal depth of profile (2). This condition is also similar to the modeling result shown in Fig. 2.19a.

### 2.5.4 Optimized Raster Orbit

A finishing liquid containing 2.3 wt %  $\text{CeO}_2$  particles (2  $\mu\text{m}$ ) was chosen. The diameter of the cylindrical nozzle in Jetting finishing was 0.95 mm. The pump pressure showed 0.4 Mpa, and the stand-off distance was 66 mm. An annular footprint with a W-shaped profile (see Fig. 2.27) was obtained for 3 min processing time.

The preceding experiment was designed to investigate the  $d/l$  with material removal, as shown in Fig. 2.28. The 0.2 mm/s linear traverse velocity of nozzle was chosen with  $d/l$ , ranging from 0.2 mm to 2.4 mm. It is obvious that the material removal has a V-shaped profile when  $d/l = 0.8$  mm, and the maximum depth  $H_{\text{Mm}}$  and width of the profile are about  $0.1702\lambda$  and 4.3 mm, respectively (see Fig. 2.28a,b,

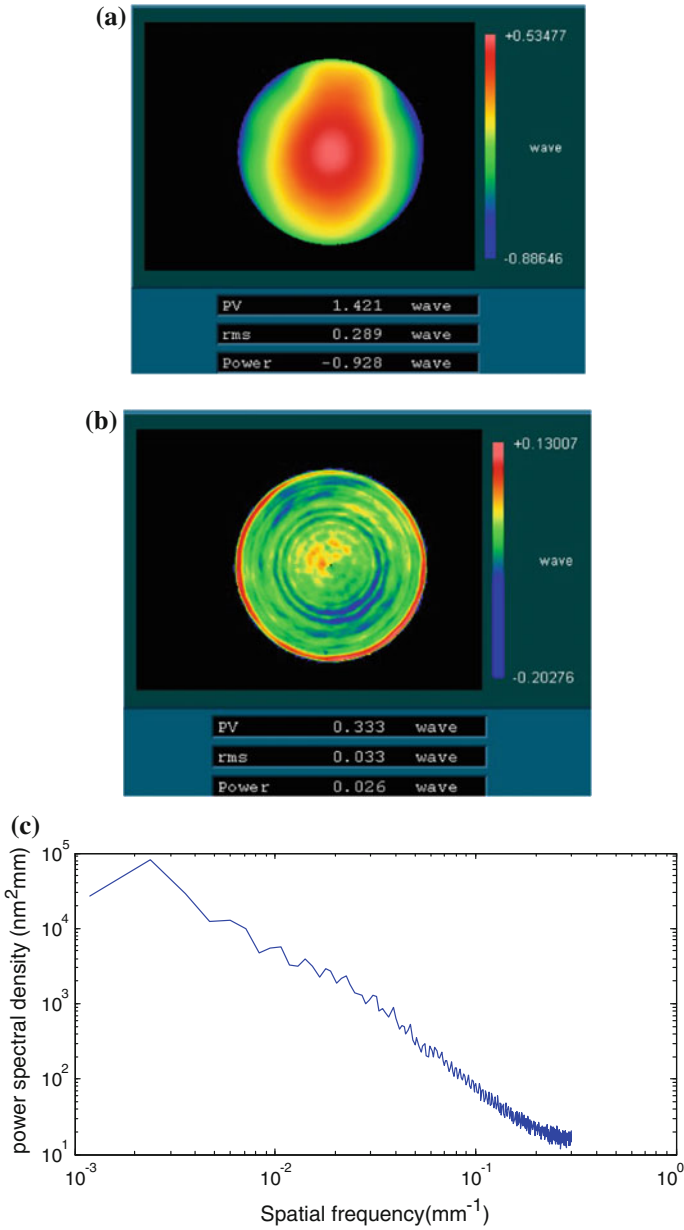


**Fig. 2.25** The finishing results of aspheric surface. **a** Initial surface error; **b** the final surface errors; **c** average PSD curve of the final surface errors

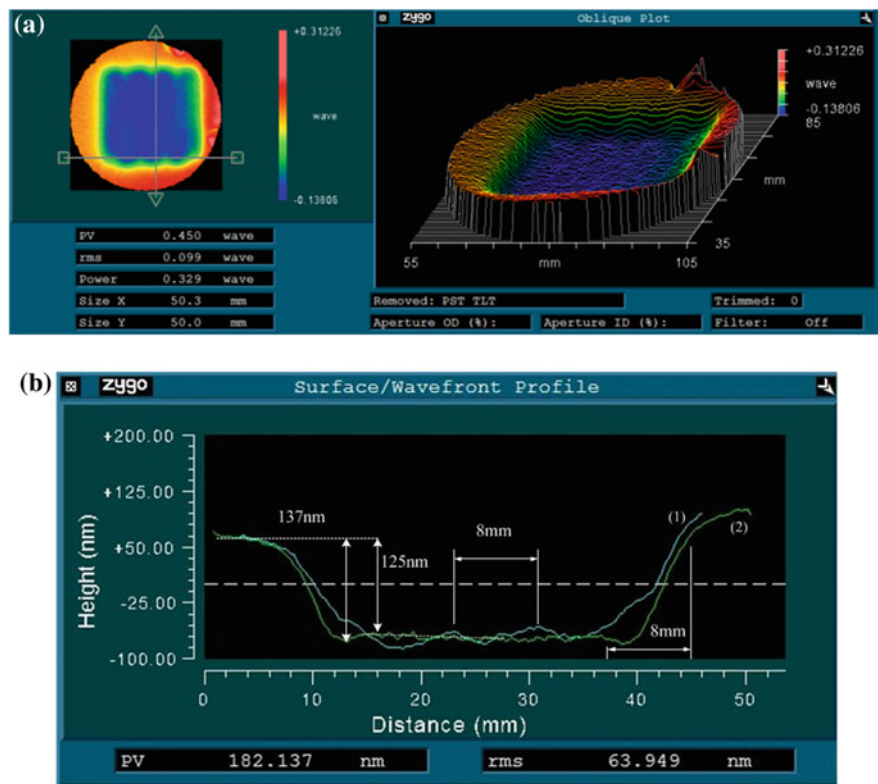


Fig. 2.26 The finishing results using raster orbit. **a** Removal map of raster orbit; **b** the profiles along the edge and the inner line orbit

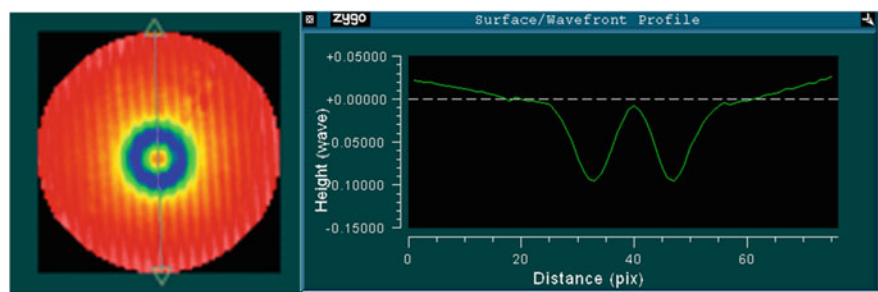
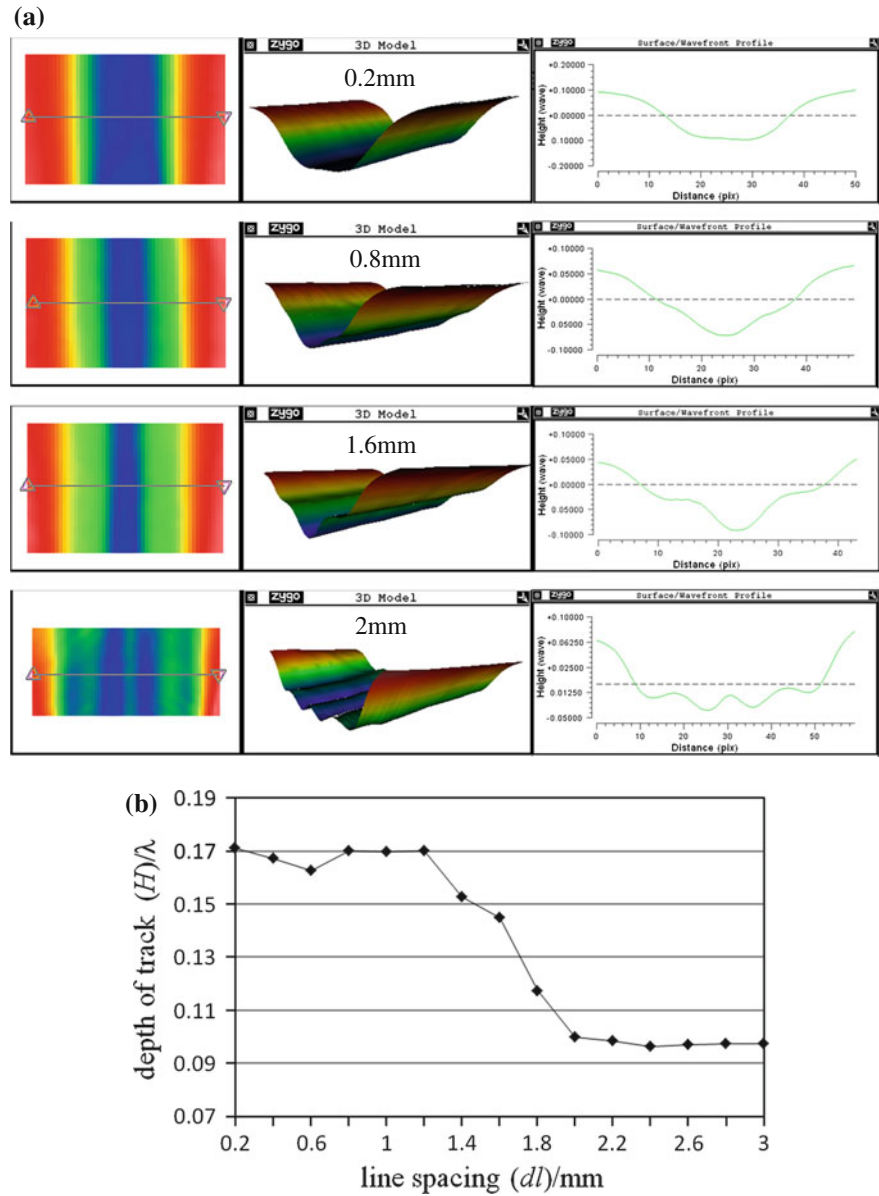


Fig. 2.27 Footprint of a nozzle on a K9 optical glass

which are similar to the curves at the same condition in Fig. 2.7). Therefore, the area  $S_M$  of the profile is about  $0.37\lambda$  (the unit of the width is 1 in area computation). On the basis of this finding, determining the corresponding Gaussian removal function (from Eq. (2.13),  $B = 7.83 \times 10^{-3} \lambda/s$ ,  $u = 0.665$ ) is easy.



**Fig. 2.28** Dependence on the  $dl$  of finishing shape. **a** Profile curves of tracks; **b** depths of tracks with different  $dl$ ; **c** V-shaped profile curves of tracks for  $dl = 0.8\text{ mm}$



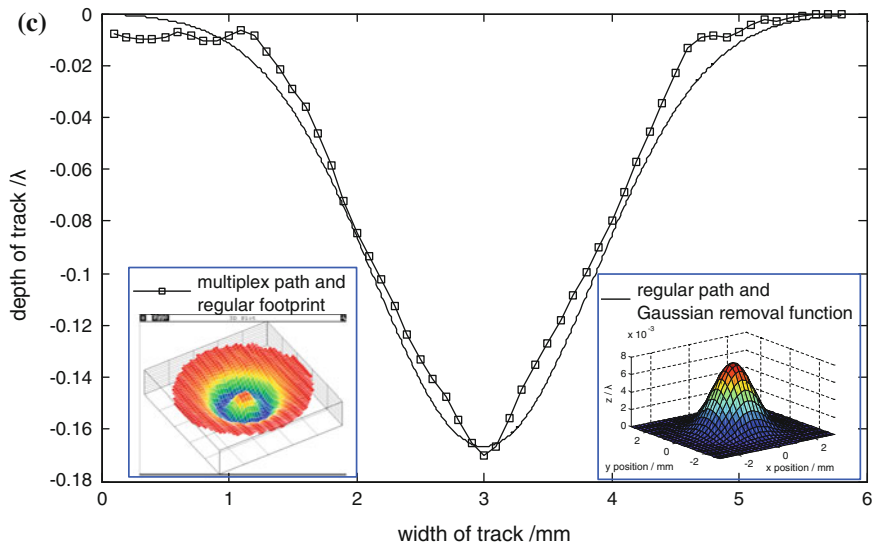


Fig. 2.28 (continued)

$$R(x, y) = 7.83 \times 10^{-3} \times \exp[-0.665 \times (x^2 + y^2)] \quad (2.26)$$

With the corresponding Gaussian removal function as expressed in Eq. (2.26), a simulation is made to obtain the distribution of track along regular orbit. Comparing to the distribution of regular footprint moving along multiplex orbit (Fig. 2.28a,  $dl = 0.8$  mm), it is important to notice that profiles possess the similar shapes as shown in Fig. 2.28c. Considering the convergence efficiency of finishing and the diameter of the corresponding Gaussian removal function (Fig. 2.28c, approach to 6 mm), the line spacing of the target orbit ( $d = 2$  mm) is adopted for multiplex orbit.

According to the above analysis, the parameters for finishing processing are exhibited in Table 2.3.

The scanning target orbit ( $d = 2$  mm, diameter of coverage area is 26 mm) was applied for the finishing of a 23 mm diameter plane K9 optical glass, with form errors of  $0.256\lambda$  (PV) and  $0.068\lambda$  (RMS) measured by a Zygo GPI interferometer (see Fig. 2.29a). Based on the target orbit, the scanning multiplex orbit with the finishing parameters (in Table 2.3,  $d_1 = d_2 = dl/2 = 0.4$  mm,  $dl = 0.8$  mm) was selected for finishing (see Fig. 2.29b).

After computing for the dwell-time by using the corresponding Gaussian removal function, the figure of initial surface and the target orbit, the velocity function on the multiplex orbit can be obtained. In the processing experiments, the finishing tool, possessing M-shaped removal function, travels along the multiplex orbit with the velocity function. After three iterations, finishing process delivers a surface waviness improvement from  $0.256\lambda$  (PV) and  $0.068\lambda$  (RMS) down to  $0.038\lambda$  (PV) and  $0.005\lambda$  (RMS) (Fig. 2.30a). Figure 2.30b, c show the average PSD curves along

**Table 2.3** Parameters of finishing processing

Parameter	Value
Mass fraction of CeO <sub>2</sub> particles in fluid (%)	2.3
Diameter of CeO <sub>2</sub> particle (μm)	2
Diameter of nozzle (mm)	0.95
Pressure (MPa)	0.4
Stand-off distance (mm)	66
Peak of corresponding Gaussian removal function ( <i>B</i> ) (λ/s)	$7.83 \times 10^{-3}$
Parameter of corresponding Gaussian removal function ( <i>u</i> )	0.665
Line spacing of the target orbit ( <i>d</i> ) (mm)	2
Value of <i>d</i> <i>l</i> in multiplex orbit (mm)	0.8

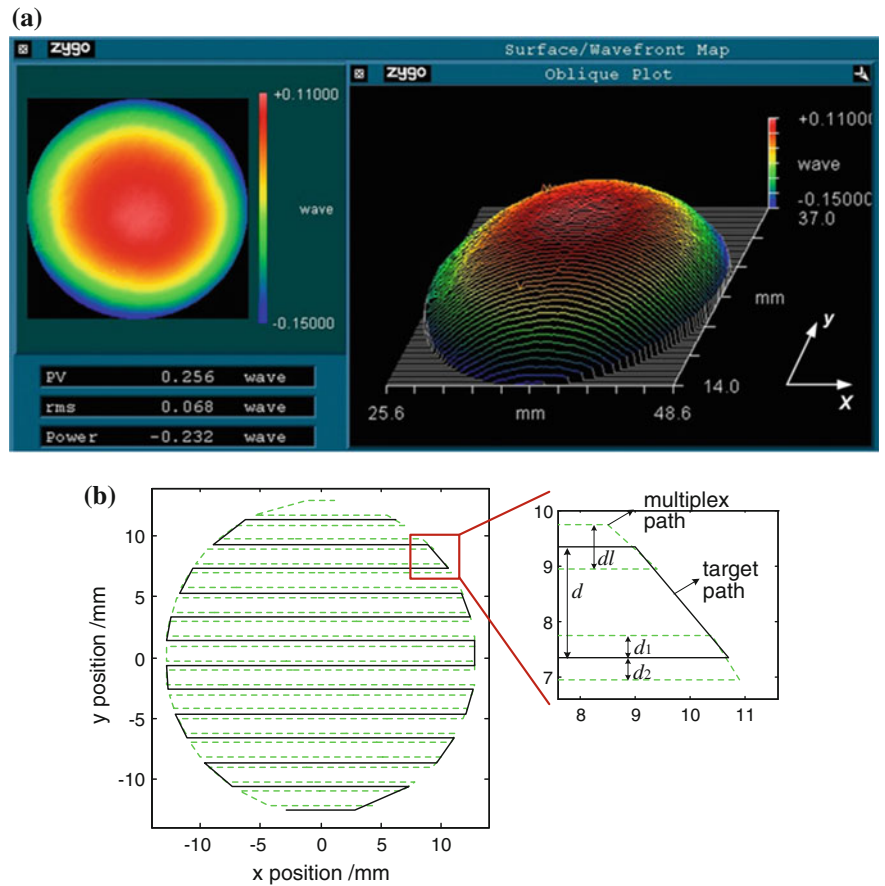


**Fig. 2.29** Process experiments with grid multiplex-orbit. **a** Original form error; **b** multiplex orbit

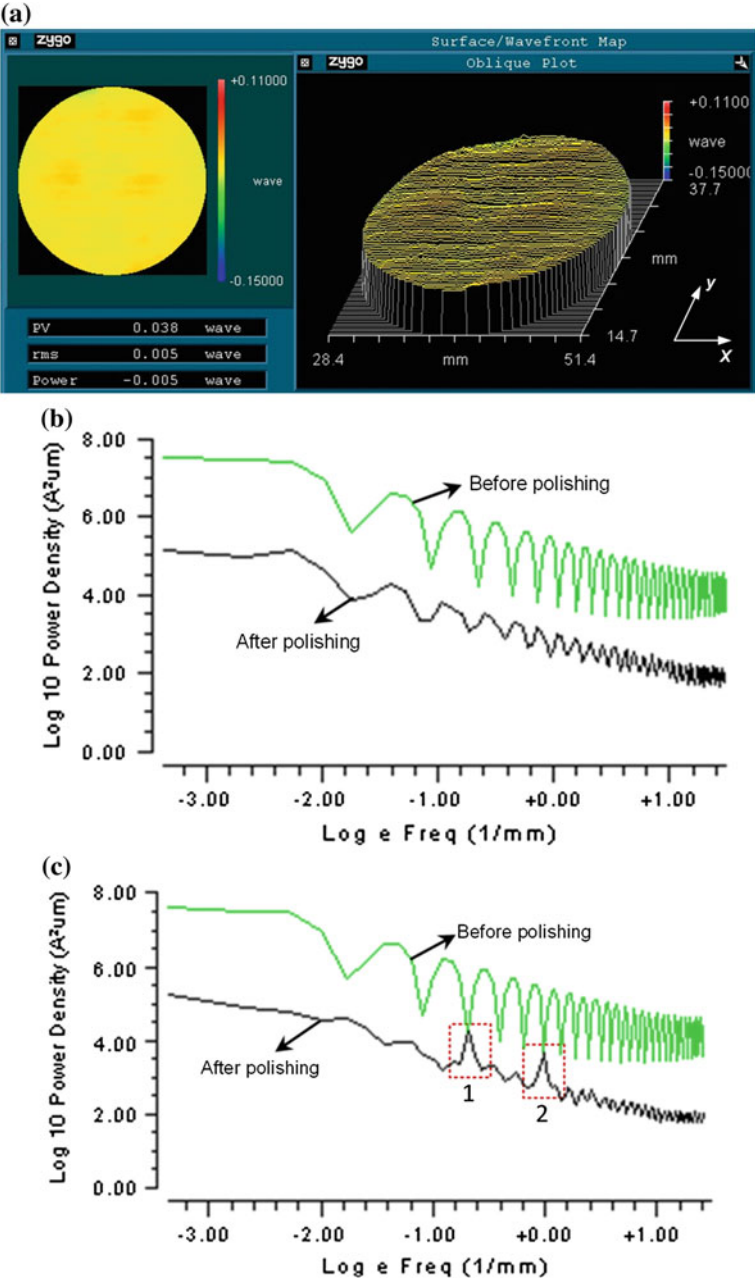


**Fig. 2.30** The finishing results. **a** Final form error results; **b** average PSD curves along *x* direction; **c** average PSD curves along *y* direction

$x$  (horizontal) and  $y$  (vertical) directions, respectively. Contrasting the PSD curves, there are mass of spatial frequency errors before finishing, which indicated that the spatial frequency errors are suppressed well. Moreover, there are two small peaks (in parts 1 and 2, see Fig. 2.30c) in the PSD curves along  $y$  direction of final surface. For one peak in the part 1, the PSD of the finished surface is approximately equal to that of before finishing with about 0.5 (1/mm) spatial frequency (see Fig. 2.30c). For the other peak in the part 2, the spatial frequency is about 1 (1/mm) frequency (Fig. 2.30c). These indicate that the spatial frequencies of the finished surface are mainly induced by the line spacing of target orbit ( $d = 2$  mm). The case of surface fabrication verifies that the multiplex orbit is effective and valid. In addition, the figure of the final surface is very homogeneous near the edge of the work-piece. This result is deceptive because there is no edge effect.

## References

1. Rupp WJ (1971) Conventional optical polishing techniques. *J Mod Opt* 18(1):1–16
2. Aspden R, McDonough R, Nitchie JF (1972) Computer assisted optical surfacing. *Appl Opt* 11(12):2739–2747
3. Cheng HB, Feng ZJ, Wu YB (2004) Fabrication of off-axis aspherical mirrors with loose abrasive point-contact machining. *Key Eng Mater* 257:153–158
4. Cheng HB, Feng ZJ, Cheng K, Wang YW (2005) Design of a six-axis high precision machine tool and its application in machining aspherical optical mirrors. *Int J Mach Tools Manuf* 45(9):1085–1094
5. Walker D, Brooks D, King A, Freeman R, Morton R, McCavana G, Kim SW (2003) The ‘Precessions’ tooling for polishing and figuring flat, spherical and aspheric surfaces. *Opt Express* 11(8):958–964
6. Walker DD, Freeman R, Morton R, McCavana G, Beaucamp A (2006) Use of the ‘Precessions’™ process for prepolishing and correcting 2D and 2½D form. *Opt Express* 14(24):11787–11795
7. Zeuner M, Kiontke S (2012) Ion Beam Figuring Technology in Optics Manufacturing. *Opt Photonik* 7(2):56–58
8. Demmler M, Zeuner M, Luca A, Dunger T, Rost D, Kiontke S, Krüger M (2011) Ion beam figuring of silicon aspheres. In: *Proceeding of SPIE, California*. 793416-793416-6
9. Kordonski W, Gorodkin S (2011) Material removal in magnetorheological finishing of optics. *Appl Opt* 50(14):1984–1994
10. Cheng HB, Feng ZJ, Wu YB (2004) Process technology of aspherical mirrors manufacturing with magnetorheological finishing. *Mater Sci Forum* 471(6):6–10
11. Cheng HB, Feng JZ, Wang Y, Lei S (2005) Magnetorheological finishing of SiC aspheric mirrors. *Mater Manuf Processes* 20(6):917–931
12. Cheng HB, Tam HY, Wang Y (2009) Experimentation on MR fluid using a 2-axis wheel tool. *J Mater Process Technol* 209(12):5254–5261
13. Cheng H, Feng Y, Ren L, To S, Wang YT (2009) Material removal and micro-roughness in fluid-assisted smoothing of reaction-bonded silicon carbide surfaces. *J Mater Process Technol* 209(9):4563–4567
14. Kordonski WI, Shorey AB, Tricard M (2006) Magnetorheological jet (MR Jet™) finishing technology. *J Fluids Eng* 128(1):20–26

15. Tricard M, Kordonski W, Shorey A, Evans C (2006) Magnetorheological jet finishing of conforal, freeform and steep concave optics. *CIRP Annals-Manufacturing Technol* 55 (1):309–312
16. Kordonski W, Shorey A (2007) Magnetorheological (MR) Jet Finishing Technological. *J Int Mat Syst Struct* 18(12):112701130
17. Wang YT, Cheng HB, Chen Y, Feng YP, Dong ZC, Tam HY (2013) Correction of remounting errors by masking reference points in small footprint polishing process. *Appl Opt* 52(33):7851–7858
18. Booij SM, Fa OW, Van BH, Braat JJ (2002) Nanometer deep shaping with fluid jet polishing. *Opt Eng* 41(8):1926–1931
19. Fang H, Guo P, Yu J (2006) Optimization of the material removal in fluid jet polishing. *Opt Eng* 45(5):053401-053401-6
20. Wang T, Cheng HB, Dong ZC, Tam HY (2013) Removal character of vertical jet polishing with eccentric rotation motion using magnetorheological fluid. *J Mater Process Technol* 213 (9):1532–1537
21. Jourdain R, Castelli M, Morantz P, Shore P (2012) Plasma surface figuring of large optical components. In: *Proceeding of SPIE, Brussels*. 843011-843011-6
22. Tam HY, Cheng HB (2010) An investigation of the effects of the tool path on the removal of material in polishing. *J Mater Process Technol* 210(5):807–818
23. Tam HY, Lui CH, Alberet CK (1999) Robotic polishing of free-form surfaces using scanning paths. *J Mater Process Technol* 95(1):191–200
24. Lartigue C, Thiebaut F, Maekawa T (2001) CNC tool path in terms of B-spline curves. *Comput Aided Des* 33(4):307–319
25. Hauth S, Linsen L (2012) Cycloids for polishing along double-spiral toolpaths in configuration space. *Int J Adv Manufact Technol* 60(1–4):343–356
26. Rososhansky M (2011) Coverage based tool-path planning for automated polishing using contact mechanics theory. *J Manufact Syst* 30:144–153
27. Hull T, Riso MJ, Barentine JM, Magruder A (2012) Mid-spatial frequency matters: examples of the control of the power spectral density and what that means to the performance of imaging systems. In: *Proceeding of SPIE, Baltimore*. 835329-835329-17
28. Filhaber J (2013) Mid-spatial-frequency errors: the hidden culprit of poor optical performance. *Laser Focus World* 49(8):32
29. Tamkin JM, Milster TD, Dallas W (2010) Theory of modulation transfer function artifacts due to mid-spatial-frequency errors and its application to optical tolerancing. *Appl Opt* 49 (25):4825–4835
30. Jester P, Menke C, Urban K (2012) Wavelet methods for the representation, analysis and simulation of optical surfaces. *IMA J Appl Math* 77(4):495–515
31. Dunn CR, Walker DD (2008) Pseudo-random tool paths for CNC sub-aperture polishing and other applications. *Opt Express* 16(23):18942–18949
32. Nelson JD, Gould A, Klinger C, Mandina M (2011) High frequency and random motion rapidly smoothes optical surfaces. *Laser Focus World* 47(10):71–74
33. Liao D, Yuan Z, Tang C, Xie R, Chen X (2013) Mid-Spatial Frequency Error (PSD-2) of optics induced during CCOS and full-aperture polishing. *J Eur Opt Soc Rapid Pub* 8:13031-1-5
34. Yu G, Li H, Walker D (2011) Removal of mid spatial-frequency features in mirror segments. *J Eur Opt Soc Rapid Pub* 6:11044-1-4
35. Zheng D, Lu F, Zhang LZ, Shi YJ (2012) The effect of polishing tool path on polishing parameters. *Appl Mech Mater* 101:1043–1046

**Pose-varied Multi-axis Optical Finishing Systems**

**Theory and Process Validation**

Cheng, H.

2015, XI, 154 p. 128 illus., 51 illus. in color., Hardcover

ISBN: 978-3-662-44181-7